Article

Molecularly Imprinted Polymer Functionalized $Bi_2S_3/Ti_3C_2T_X$ MXene Nanocomposites for Photoelectrochemical/ Electrochemical Dual-Mode Sensing of Chlorogenic Acid

Zhenli Qiu [1], Dechun Fan [1], Xianghang Xue [1], Shujun Guo [1], Youxiu Lin [2], Yiting Chen [1,*] and Dianping Tang [3,*]

[1] College of Materials and Chemical Engineering, Minjiang University, Fuzhou 350108, China; zhenliqiu@mju.edu.cn (Z.Q.); N191827009@fzu.edu.cn (D.F.); 200627085@fzu.edu.cn (X.X.); 2527@mju.edu.cn (S.G.)
[2] Key Laboratory of Modern Analytical Science and Separation Technology of Fujian Province, College of Chemistry, Chemical Engineering and Environment, Minnan Normal University, Zhangzhou 363000, China; lyx1817@mnnu.edu.cn
[3] Key Laboratory of Analytical Science for Food Safety and Biology (MOE & Fujian Province), Department of Chemistry, Fuzhou University, Fuzhou 350108, China
* Correspondence: cyt@mju.edu.cn (Y.C.); dianping.tang@fzu.edu.cn (D.T.)

Abstract: We report the proof-of-concept of molecularly imprinted polymer (MIP) functionalized $Bi2S_3/Ti_3C_2T_X$ MXene nanocomposites for photoelectrochemical (PEC)/electrochemical (EC) dual-mode sensing of chlorogenic acid (CGA). Specifically, the in-situ growth of the $Bi_2S_3/Ti_3C_2T_X$ MXene served as a transducer substrate for molecularly imprinted polymers such as PEC and EC signal generators, due to its high surface area, suitable bandwidth and abundant active sites. In addition, the chitosan as a binder was encapsulated into MIP by means of phase inversion on a fluorine-doped tin dioxide (FTO) electrode. In the determination of CGA as an analytical model, the dual-mode sensor based on MIP functionalized $Bi_2S_3/Ti_3C_2T_X$ MXene nanocomposites had good selectivity, excellent stability and acceptable reproducibility, which displayed a linear concentration range from 0.0282 μM to 2824 μM for the PEC signal and 0.1412 μM to 22.59 μM for the EC signal with a low detection limit of 2.4 nM and 43.1 nM, respectively. Importantly, two dual-response mode with different transduction mechanisms could mutually conform to dramatically raise the reliability and accuracy of detection compared to single-mode detection. This work is a breakthrough for the design of dual-mode sensors and will provide a reasonable basis for the construction of dual-mode sensor platforms.

Keywords: $Bi_2S_3/Ti_3C_2T_X$ MXenes; dual-model; photoelectrochemical; electrochemical; molecularly imprinted polymers; chlorogenic acid

1. Introduction

The photoelectrochemical (PEC) sensing platform is an integration of the electrochemical sensor and photoelectric conversion process, which has attracted a lot of researchers' growing attention [1–3]. As a novel and prospective analytical technology, it has intrinsic merits of negligible background signals, fast response time, high sensitivity, good selectivity, and flexible instrument device due to the separation of light source and electrochemical detection [4]. Then, it has been widely applied for quantification in chemical, biomedical and environmental fields [5]. However, the accuracy of a PEC platform relying on single-mode detection cannot be guaranteed, which suffers from external interferents, such as the fluctuation of testing environment, the influence of different instruments and different personnel operation [6,7]. Thus, there is an urgent need for a separate signal that possesses a totally independent transmission path, which improves the accuracy and sensitivity of the proposed strategy. In recent years, a number of dual-mode biological detection

strategies have been reported, in which two independent signal transductions from different mechanisms can calibrate the systematic errors or background signals, and mutually verify dual responses, such as electrochemiluminescence (ECL)-electrochemical (EC) [8], ECL-colorimetry [9], PEC-fluorescence [10], PEC-colorimetry [11] and chemiluminescence-PEC strategies [12]. In these dual-mode platforms, the PEC-EC strategy requires only one electrochemical instrument to achieve two signal readouts on the same probe, optimizing the sensing interface and reducing uncontrollable changes. To construct high performance PEC-EC dual-mode sensing, it is important to design a multifunctional signal transmitter with PEC and EC readouts for a simplified sensing structure. Generally speaking, the core element of the sensor includes materials and recognition probes. For a PEC signal, it is efficient photoelectric conversion based on photosensitive material [13], i.e., hollow In_2O_3–In_2S_3 [14], $AuNPs/Cs_3Bi_2Br_9$ QDs/BiOBr [15] and In_2S_3/WO_3 heterojunction [16] presented efficient PEC performance for biosensors, whereas for an EC signal, suitable electrocatalytic materials can obtain a sensing model with high sensitivity [17], such as Au-Based nanocomposites [18], two-dimensional nanomaterials [19] and metal-organic frameworks (MOFs) [20]. Therefore, the selection of materials with high photosensitivity, conductivity and electrocatalytic properties is crucial to the development of PEC-EC dual-mode sensors for the ideal signals acquisition.

As a new kind of two-dimensional transition metal material, MXene has been widely reported due to its ultrathin structure and excellent physical and chemical properties [21]. It will be obtained from the MAX phase by etching Al, where M represents the early transition-metal, A usually belongs to IIIA or IVA element, and X refers to C or N element. $Ti_3C_2T_X$, as the first typical MXene, has various merits including a huge special dynamic area, practical metal conductivity, highly adaptable band gap, good biocompatibility and proper optical and mechanical execution [22]. Furthermore, it is noteworthy that the OH-functionalized $Ti_3C_2T_X$ MXene can effectively separate photocarriers and transport photogenerated carriers to the $Ti_3C_2T_X$ MXene/semiconductor heterojunction to form Schottky junction due to the difference between valence band and Fermi level (EF) [23]. It also allows the intrinsic electric field between $Ti_3C_2T_X$ MXene and photosensitive materials such as semiconductors to ascend. In contrast to other narrow bandwidth semiconductors, bismuth sulfide (Bi_2S_3) was being considered as a potential semiconductor material due to its unique features such as n-type properties, reasonable photoelectric conversion efficiency (5%), excellent biocompatibility and high absorptivity coefficient ($\lambda \leq 800$ nm) [24]. We believe that the heterojunction arrangement between Bi_2S_3 and $Ti_3C_2T_X$ MXene might induce a self-driven charge transport channel at the interface due to the well-matched energy levels of Bi_2S_3 and $Ti_3C_2T_X$ MXene, which would accelerate charge transmission and suppress the recombination of electron-hole pairs at those interfaces. MXene-based composites have the potential to construct PEC/EC dual-signal biosensing platforms because of their structural tunability and possible excellent photoactivity and electrochemical activity.

To achieve the applicability of the PEC/EC dual-mode biosensor, the recognition element also plays a crucial role [25]. Usually, the intimate fixation of molecules might bring some inherent disadvantages, such as being time consuming, complex interface modifications and poor reproducibility. Compared to other expensive biomolecule recognition units (aptamer, antibody and peptide), molecular imprinting is an effective technique for simulating molecular recognition through molecularly imprinted polymers (MIPs) called artificial receptors [26,27]. MIP is formed by copolymerization of template molecules (targets) and functional monomers, which are then removed to produce the memory cavities toward the target with complementary shapes, sizes and functions [28]. The memory cavities can recognize the target by "locking and bonding" mechanisms [29]. Molecular imprinting is a low-cost and simple identification method, which facilitates interface simplification for dual-mode detection.

In this work, we reported a novel MIP functionalized $Bi_2S_3/Ti_3C_2T_X$ MXene nanocomposites for PEC/EC dual-mode sensing of chlorogenic acid (CGA), as shown in Scheme 1 The CGA is a phenolic acid compound, which broadly exists in vegetables and other

foods [30]. Many studies have demonstrated that CGA has a massive range of functions, such as having anti-tumor, antibacterial, antiviral, antioxidant and blood pressure-lowering blood lipid properties [31]. With these motivations, this work first prepared $Bi_2S_3/Ti_3C_2T_X$ MXene nanocomposite as a transducer substrate. Specifically, as shown in Scheme 1, the nanosheet $Ti_3C_2T_X$ MXene was prepared by etching and ultrasonic exfoliation, and the $Bi_2S_3/Ti_3C_2T_X$ MXene nanocomposite was prepared through the hydrothermal method. Then, MIP precursor was synthesized via chemical polymerization with CGA as the template, chitosan as the monomers and sulfuric acid as cross-linking agents. Subsequently, $Bi_2S_3/Ti_3C_2T_X$ MXene and MIP precursors were combined with the FTO electrode by a layer-by-layer assembly strategy with the drop coating method. After removing the CGA template, the recognition site of CGA remained on the MIP/$Bi_2S_3/Ti_3C_2T_X$ MXene electrode. In the presence of CGA, the MIP/$Bi_2S_3/Ti_3C_2T_X$ MXene electrode enhanced the steric hindrance effect and blocked the electron-hole pair conduction, resulting in photocurrent reduction. Additionally, the electrochemical signal was raised due to the electrocatalytic activity of the MIP/$Bi_2S_3/Ti_3C_2T_X$ MXene electrode towards CGA. This strategy provides a new perspective for the construction of dual-signal sensing platform and an effective improvement for enhancing the accuracy of biological analysis.
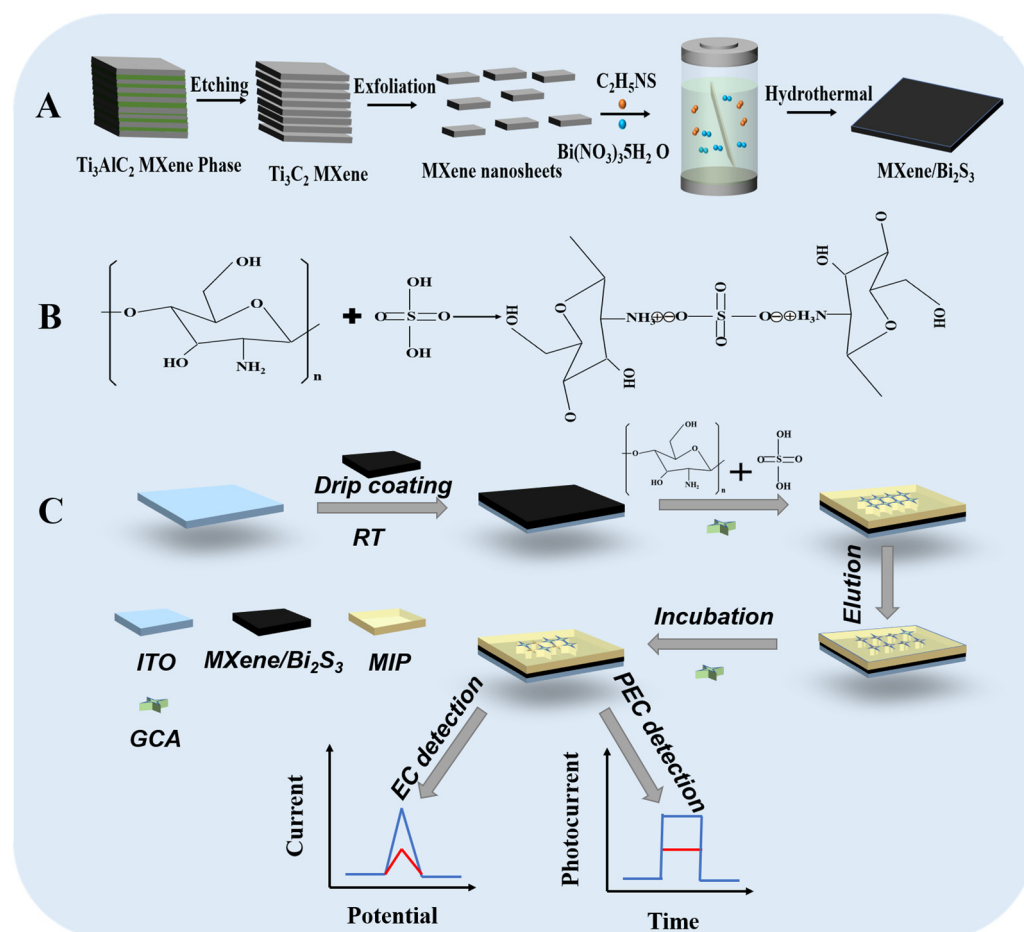
Scheme 1. Schematic illustration of (**A**) the formation process of the $Bi_2S_3/Ti_3C_2T_X$ MXene; (**B**) the mechanism of chitosan cross-linking; (**C**) the principle of MIP functionalized $Bi_2S_3/Ti_3C_2T_X$ MXene nanocomposites for PEC/EC dual-mode sensing of CGA.

2. Materials and Methods

2.1. Chemical Reagents

The chemical reagents used in the bioassay are detailed in the Supplementary Materials.

2.2. Synthesis of MXene Nanosheets

The MXene nanosheets were synthesized through a liquid-phase exfoliation method [32,33]. Briefly, 4 g of Ti_3AlC_2 powder was gently added to 40 mL of HF solution (40 wt%) with slight stirring. After etching at room temperature for 72 h, the mixture was washed with pure water and centrifuged 6 times until the pH of the solution was equal to or greater than 6. Then, the centrifuged product was dried in a vacuum oven at 40 °C. The dried product was dispersed in 25 mL of DMSO, stirred for one day at room temperature and then centrifuged and washed thoroughly with pure water several times to remove excess DMSO. After that, the MXene nanosheets solution was obtained by sonication in water for 1.5 h with N_2 atmosphere protection. After that, the product was centrifuged at 8000 rpm for 1h to remove the impurities. At last, the product was stored in a cool place for use in successive experiments.

2.3. Synthesis of Bi_2S_3/MXene Composites

The Bi_2S_3/MXene was synthesized by slightly modifying the previous method [34,35]. Then, 0.4 mM $Bi(NO_3)_3$ solution was dispersed in ultrapure water containing 1300 μL of 5 mg mL^{-1} $Ti_3C_2T_X$ nanosheet solution. Then, the mixture solution was stirred for 3 h to ensure sufficient electrostatic adsorption time. Afterwards, 54 mg of thioacetamide (C_2H_5NS) was added to the mixture solution and stirred slightly for 1 h. Next, the mixed solution was put into to a 50 mL Teflon-lined stainless-steel autoclave, which was hydrothermally kept at 160 °C for 8 h. After cooling to room temperature, the final black precipitate was washed and centrifuged with deionized water and anhydrous ethanol and dried overnight in a vacuum drying oven at 60 °C to obtain $Ti_3C_2T_X$ MXene/Bi_2S_3 composites. Choose different amounts of $Ti_3C_2T_X$ MXene to synthesize Bi_2S_3/$Ti_3C_2T_X$ MXene composites with varying ratios of MXene.

2.4. Preparation of Molecularly Imprinted Polymer-CGA (MIP-CGA) and Non-Imprinted Polymer (NIP)

Both MIP-CGA and NIP were prepared by the phase conversion method [36,37]. Briefly, 20 mg of chitosan was dissolved in 20 mL of acetic acid solution (1%, v/v) and then stirred slightly at 60 °C for 2 h to prepare the 1 mg mL^{-1} chitosan solution. To prevent swelling of the molecularly imprinted layer, 40 mg of chlorogenic acid was added to the above chitosan solution with an appropriate amount of H_2SO_4 (1.0 M) as a cross-linking agent, and continuously stirred at 60 °C for 4 h. Cross-linking was formed between the amino group in chitosan and the sulfate ion in sulfuric acid due to the Coulomb interaction, as shown in Scheme 1B. After filtering to remove impurities, the MIP-CGA membrane was sealed and stored in a cool place. The non-molecularly imprinted layer (NIP) was prepared in the same way, where the difference was that the chlorogenic acid imprinted molecules were not added.

2.5. Fabrication of the PEC and EC Electrodes

The FTO electrode (sheet resistance, 8 Ω/square) was cleaned three times with a mixture (1:1:2, $v/v/v$) of acetone, ethanol and pure water by sonication wave and dried overnight before use. Then, the perforator (Deli, No. 0102, Hangzhou, China) on tape with a 6 mm round hole, and then with a circular hole tape was pasted on the glass to control the exposure of the FTO glass area (0.28 cm^2). Later, 10 mg of Bi_2S_3/$Ti_3C_2T_X$ MXene composites powder was evenly dispersed in 2 mL of ultrapure water and sonicated for 30 min. The 20 μL of 5 mg mL^{-1} obtained solution was applied uniformly to a fixed area of the FTO glass surface and then naturally dried. Afterward, 20 μL of MIP-CGA was combined with the Bi_2S_3/$Ti_3C_2T_X$ MXene and dried naturally at room temperature.

The MIP-CGA/Bi$_2$S$_3$/Ti$_3$C$_2$T$_X$ MXene/FTO electrode was treated with ethanol (10%, *v/v*) for 20 min to remove the CGA molecule. Finally, the obtained electrodes (marked as MIP/Bi$_2$S$_3$/Ti$_3$C$_2$T$_X$ MXene/FTO) were washed several times with ultrapure water, which obtained the specific site cavities of CGA. As a control, NIP/Bi$_2$S$_3$/Ti$_3$C$_2$T$_X$ MXene/FTO electrodes were also prepared according to the above method without a CGA template.

2.6. Electrochemical and Photoelectrochemical Measurement

Firstly, the fabricated electrodes were incubated with various concentrations of CGA solution at room temperature for 1 h. The PEC signal was performed in current-time mode at a bias voltage of 0 V with a conventional three-electrode system by using the Bi$_2$S$_3$/Ti$_3$C$_2$T$_X$ MXene/FTO electrode as the working electrode, a platinum wire electrode as the auxiliary electrode, and an Ag/AgCl reference electrode. Then, the photocurrent responses were recorded using an electrochemical workstation (CH Instruments, 760D, Shanghai, China). Turn the light source on and off at a rate of 10 *s* under illumination of 500 W Xe lamp (Solar-500, Beijing NBeT Group Corp., Beijing China). The EC signal was measured using the DPV method record between 0 V and 0.7 V. The test solution was PBS solution (0.1 M, PH = 7.4). The detection sequence is to detect the PEC signal first, and then the EC signal.

3. Results

3.1. Characterization of Bi$_2$S$_3$/Ti$_3$C$_2$T$_X$ MXene Materials

The morphologies and microstructures of as-prepared samples (multilayer Ti$_3$C$_2$T$_X$, Ti$_3$C$_2$T$_X$ nanosheet, Bi$_2$S$_3$ and Bi$_2$S$_3$/Ti$_3$C$_2$T$_X$ MXene) were observed using scanning electron microscopy (SEM, Hitachi, SU8010, Japan) and transmission electron microscope (TEM, FEI, Talos F200X, USA). As shown in Figure 1A, we could clearly see the organ-like structure of Ti$_3$C$_2$T$_X$ MXene after HF corrosion, and the thickness of each layer was about tens of nanometers. Figure 1B displayed the Ti$_3$C$_2$T$_X$ nanosheets after intercalation and ultrasonic exfoliation. The Bi$_2$S$_3$ exhibited the morphology of nanorods as seen in Figure 1C, the average diameter of nanorod was approximately 50 nm and average of length was about 450 nm. The stacking of these nanorods facilitated accurate light absorption, and these small degrees facilitated carrier transport. As observed in Figure 1D, the Bi$_2$S$_3$/Ti$_3$C$_2$T$_X$ MXene showed a stacking shape, which was made up of Bi$_2$S$_3$ nanorods stacked on nanosheet layers with the large specific surface area. The Bi$_2$S$_3$/Ti$_3$C$_2$T$_X$ MXene composite was further proved using TEM. The TEM images (Figure 1E) showed that the high-level Bi$_2$S$_3$ nanorods were coated on the low-level Ti$_3$C$_2$T$_X$ MXene nanosheet, which was consistent with the SEM images. The high-resolution TEM (HRTEM) image (Figure 1F) showed the interplanar spacing between adjacent lattice fringes were 0.221 and 0.267 nm, respectively, corresponding to the crystal plane of the Bi$_2$S$_3$ (430) and the crystal plane of Ti$_3$C$_2$T$_X$ MXene (0$\bar{1}$10) [34,38]. In addition, the energy dispersive X-ray spectroscopic (EDS) mapping images (Figure 1G–I) revealed the homogeneous distributions of Bi, Ti, C, and S elements, indicating the successful combination of Bi$_2$S$_3$ and Ti$_3$C$_2$T$_X$.

During the preparation process, the Bi$_2$S$_3$ was in-situ grown on the surface of the Ti$_3$C$_2$T$_X$ MXene nanosheets. The electrostatic interaction between the two components was verified by the measured Zeta potential (Figure S1a–d in Supplementary Materials). First, due to the negative charge of Ti$_3$C$_2$T$_X$ nanosheets (column 'b'), the electrical interaction occurred between Bi^{3+} (column 'a') and the Ti$_3$C$_2$T$_X$ surface. Then, the Bi$_2$S$_3$/Ti$_3$C$_2$T$_X$ MXene (column 'd') were formed during the hydrothermal process, and the Zeta potential of Bi$_2$S$_3$/Ti$_3$C$_2$T$_X$ MXene changed from −25 V to 18 V. It was proved that Bi$_2$S$_3$ could spontaneously form on the surface of Bi$_2$S$_3$/Ti$_3$C$_2$T$_X$ MXene by electrostatic adsorption, and the agglomeration and re-stacking of Ti$_3$C$_2$T$_X$ nanosheets were avoided.
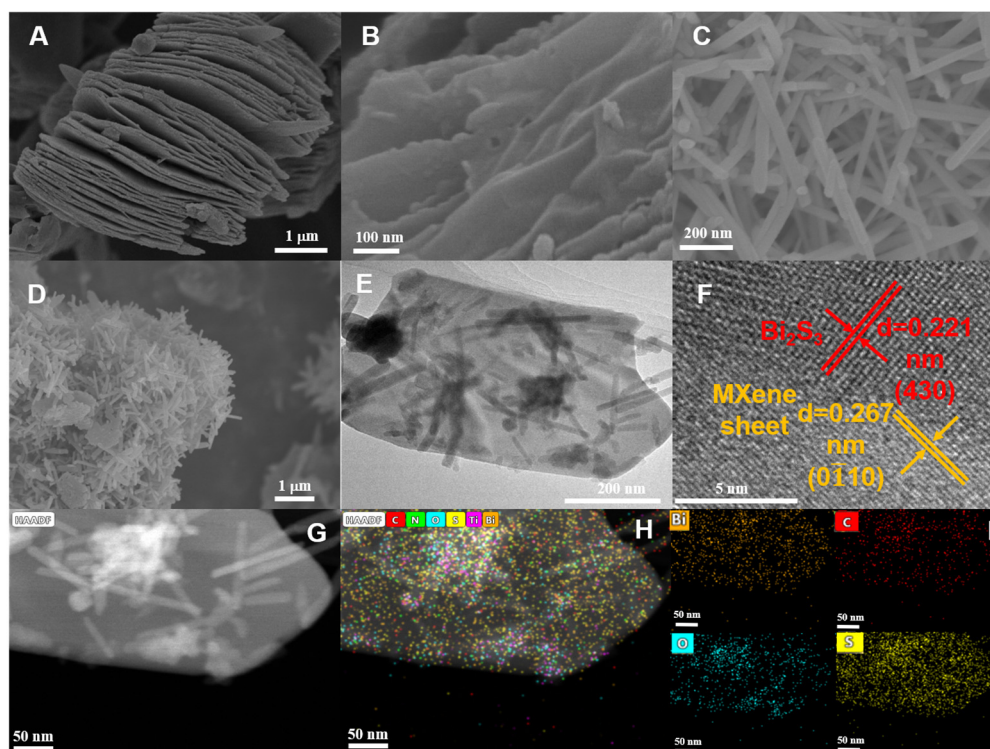
Figure 1. SEM images of (**A**) organ-like $Ti_3C_2T_X$ MXene; (**B**) $Ti_3C_2T_X$ MXene nanosheet; (**C**) Bi_2S_3 and (**D**) $Bi_2S_3/Ti_3C_2T_X$ MXene nanosheet; (**E**) TEM image of $Bi_2S_3/Ti_3C_2T_X$ MXene; (**F**) HRTEM images of $Bi_2S_3/Ti_3C_2T_X$ MXene; (**G**) HAADF image and (**H**,**I**) EDS mappings of $Bi_2S_3/Ti_3C_2T_X$ MXene.

The crystal structure of $Bi_2S_3/Ti_3C_2T_X$ MXene were further investigated by the X-ray diffraction (XRD, Rigaku, Miniflex, Japan) spectra. Figure 2A revealed that $Ti_3C_2T_X$ had diffraction peaks at 9° and 61°, which belonged to (002) and (110) planes of $Ti_3C_2T_X$ MXene, respectively [39]. The XRD patterns of $Bi_2S_3/Ti_3C_2T_X$ MXene indicated that these peaks contained the characteristic peaks of pristine Bi_2S_3 and $Ti_3C_2T_X$ MXene [40,41]. In addition, the composites did not destroy the crystal phase of the individual material. Signals of Ti, C, Bi and S elements were detected on $Bi_2S_3/Ti_3C_2T_X$ through the full spectrum of X-ray photoelectron spectroscopy (XPS, Thermo Fisher Scientific, Verios G 4UC, USA), as shown in Figure 2B. The C 1s spectrum (Figure 2C) exhibited four peaks, corresponding to the C-C, C-O, Ti-C and O=C-O bonds, respectively [42,43]. Moreover, four peaks attributed to Bi $4f_{7/2}$ and Bi $4f_{5/2}$ can be found in the Bi 4f spectrum (Figure 2D). The peaks at 158.4 eV and 164.7 eV indicated the presence of Bi-O bonds, which may be due to the reaction of Bi_2S_3 with the oxide-containing groups of the $Ti_3C_2T_X$ MXene [35,44]. In addition, the S 2p spectrum included two peaks that could be assigned to S $2p_{3/2}$ and S $2p_{1/2}$, respectively [35,44]. The O 1s spectrum showed three peaks (Figure 2E), which could be attributed to O–Bi, Ti–O and O=C functional groups in $Bi_2S_3/Ti_3C_2T_X$ MXene, respectively. As shown in Figure 2F, the $Bi_2S_3/Ti_3C_2T_X$ MXene only showed two Ti speaks (Ti-O and Ti-C), indicating the Ti-O bond derived from the oxygen-containing functional surface attached to MXene [35,44]. These results confirmed that there was a strong interfacial interaction between $Ti_3C_2T_X$ and Bi_2S_3. When $Ti_3C_2T_X$ and Bi_2S_3 were in close contact, the local electron density of Bi and S decreased, and the electron density of one Ti increased, and the subsequent electrons transferred from Bi_2S_3 to $Ti_3C_2T_X$. Therefore, an internal electric field can be formed at the interface of $Ti_3C_2T_X$ and Bi_2S_3.

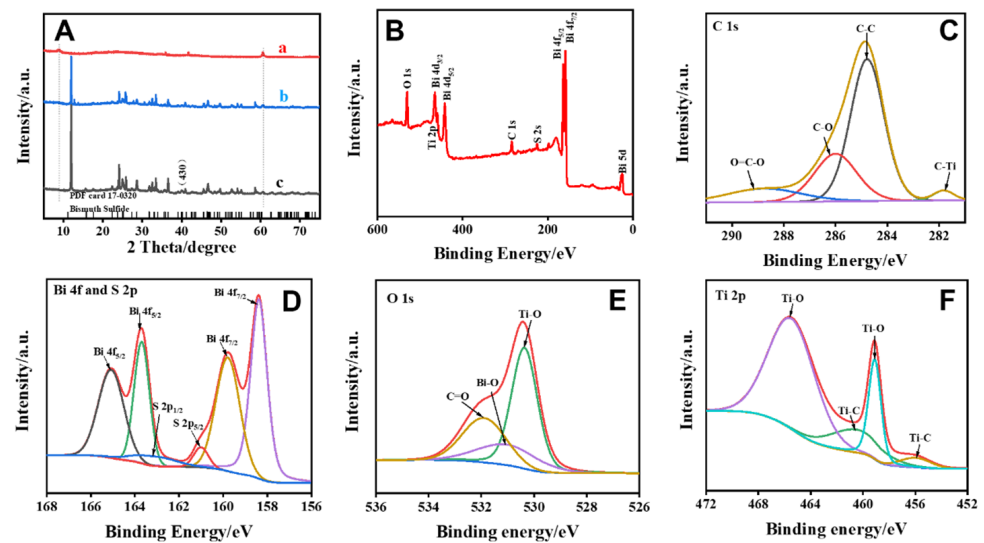**Figure 2.** (**A**) XRD patterns of (a) $Ti_3C_2T_X$ MXene, (b) $Bi_2S_3/Ti_3C_2T_X$ MXene nanosheet and (c) Bi_2S_3; (**B**) XPS survey spectra analysis of $Bi_2S_3/Ti_3C_2T_X$ MXene; High-resolution XPS spectra of (**C**) C 1s; (**D**) Bi 4f; (**E**) O 1s and (**F**) Ti 2p.

3.2. PEC Properties of $Bi_2S_3/Ti_3C_2T_X$ MXene Composites

The PEC properties of different photoactive materials were investigated by recording the photocurrent response under xenon lamp light irradiation. As shown in Figure 3A, the photocurrent response of $Ti_3C_2T_X$ (curve 'a') was 23 nA. The Bi_2S_3 material (curve 'b') had a small photocurrent signal (319 nA) due to the narrow bandgap. It could be clearly seen that the photocurrent of the $Bi_2S_3/Ti_3C_2T_X$ MXene composite material (curve 'c') enhanced by a large margin and had better photoelectric properties. These results indicated that the internal electric field of $Bi_2S_3/Ti_3C_2T_X$ MXene had a positive effect on the separation and transfer of electron hole pairs [34,45].
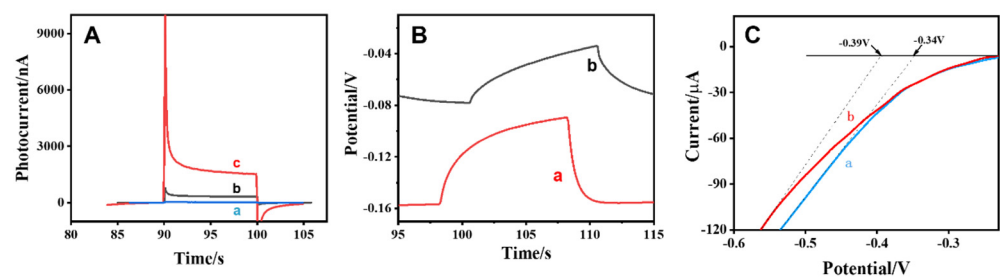

Figure 3. (**A**) Photocurrent responses of (a) $Ti_3C_2T_X$ (b) Bi_2S_3 and (c) Bi_2S_3/Ti_3C_2T; (**B**) OCP response of (a) Bi_2S_3 and (b) $Bi_2S_3/Ti_3C_2T_X$ MXene; (**C**) LSV responses of (a) $Bi_2S_3/Ti_3C_2T_X$ and (b) Bi_2S_3.

To further explore the PEC properties of $Bi_2S_3/Ti_3C_2T_X$ MXene, the open circuit potential (OCP) and the linear sweep voltammetry (LSV) were used to investigate the differences of material. Figure 3B showed that the OCP of Bi_2S_3 (curve 'a') and $Bi_2S_3/Ti_3C_2T_X$ MXene (curve 'b') both shifted to higher potentials under irradiation, indicating that these two materials possessed an effective hole transfer capability [46,47]. Higher OCP (OCP = $OCP_{light\ off}$ − $OCP_{light\ on}$) implied better electronic conductivity at the electrode–electrolyte interface. Among them, the OCP potential of $Bi_2S_3/Ti_3C_2T_X$ composite was significantly higher, which indicated that the built-in electric field formed by the combination of Bi_2S_3 and $Ti_3C_2T_X$ had strong electron-hole separation ability. Furthermore, the LSV results (Figure 3C) revealed that the $Bi_2S_3/Ti_3C_2T_X$ MXene composites (−0.34 V vs. Ag/AgCl) were higher than that of Bi_2S_3 (−0.39 V vs. Ag/AgCl). The results showed that

$Ti_3C_2T_X$ MXene promoted electron migration and improved ability of electrons scavenging [48]. These results were consistent with the phenomenon of photocurrent response.

3.3. Feasibility of PEC/EC Dual-Modal Sensing Platform

In addition, Fourier transform infrared (FT-IR) spectrum was obtained from Figure S2A,B, which verified the successful preparation of the CGA-affinity molecularly imprinted film. As can be seen in Figure S2A, the characteristic peaks of CS (curve 'a') at approximately 3474 cm^{-1} and 2937 cm^{-1} belonged to the N-H stretching vibrations and the C-H stretching vibration. The peaks of 1664 cm^{-1} and 1265 cm^{-1} represented C=O stretching (amide I) and C-N stretching (amide III), respectively [49]. The characteristic peak at 1589 cm^{-1} was the N-H bending of primary amines. The characteristic peaks of 1157 cm^{-1}, 1081 cm^{-1} and 894 cm^{-1} were inferred as C-O-C bridges, asymmetric stretching C=O and typical stretching vibrations of the pyranose ring, respectively [50]. Compared with native CS, the characteristic band near 3400 cm^{-1} disappeared in MIP (curve 'c'), which belonged to N-H stretching vibration peak of primary amine [51,52]. This indicated that the sulfate radical of sulfuric acid reacted with the amino group of chitosan. The absorption peak at around 2136 cm^{-1} in MIP was the characteristic peak of NH^{3+}, which further indicated the protonation process of sulfuric acid and chitosan film, forming the structure of NH^{3+}-$SO4^{2-}$-NH^{3+} [36]. The results of FTIR spectroscopy showed that MIP was successfully prepared by chemical polymerization.

In order to further explore the feasibility of the sensor, the photocurrent response of different modified electrodes was compared. In Figure 4A, compared with the other modified electrodes, the Bi_2S_3/MXene electrode (curve 'a') exhibited a more robust photocurrent response. After the MIP-CGA was modified on the surface of the Bi_2S_3/MXene electrode (curve 'b'), the photocurrent response was significantly reduced because the MIP-CGA hindered the electron conduction on the electrode surface. After removing the CGA template (curve 'c'), the photocurrent increased to a large extent. It showed that imprinting sites were formed in the molecularly imprinted layer after elution, which enhanced the electron conductivity and lead to a significant increase in the photocurrent response [29]. After incubation with the CGA (curve 'd'), the photocurrent response decreased to varying degrees, indicating that the CGA molecules were recombined with the imprinting sites on the electrode [53]. In addition, after the elution of NIP/Bi_2S_3/MXene and MIP/Bi_2S_3/MXene, the photocurrent of the NIP/Bi_2S_3/MXene hardly changed, whereas MIP/Bi_2S_3/MXene significantly changed (Figure 4B). This consequence could be explained that the absence of CGA molecules in NIP/Bi_2S_3/MXene lead to no cavity formation with the eluent, resulting in little change in the photocurrent, whereas MIP/Bi_2S_3/MXene eluted CGA, resulting in cavities on the surface and enhancing the efficiency of electron conduction.

The DPV current response was used to compare the situation of different modified electrodes. In Figure 4C, the Bi_2S_3/MXene electrode (curve 'a') basically had no DPV signals. After the surface of Bi_2S_3/MXene electrode was modified with MIP-CGA (curve 'b'), the DPV signal was greatly enhanced due to the electrocatalytic activity of CGA in MIP. After removing the CGA template (curve 'c'), the DPV signal was greatly reduced due to the elution of the CGA with electrocatalysis active in the MIP. After incubation with CGA (curve 'd'), the DPV signal was significantly enhanced, which indicated that the CGA molecule was bound to the imprinted site on the electrode, and the MIP/Bi_2S_3/MXene electrode enhanced the electrocatalysis of CGA [54,55]. From Figure 4D, CGA still had the DPV signal without Bi_2S_3/MXene substrate material (curve 'a'). Surprisingly, DPV signals in the presence of Bi_2S_3/MXene substrate material increased significantly compared to DPV signals in the absence of Bi_2S_3/MXene substrates (curve 'b'). It showed that Bi_2S_3/MXene had a driving effect on the electrocatalysis of CGA. Therefore, all the research results together verified the feasibility of PEC/EC dual-modal sensing platform.
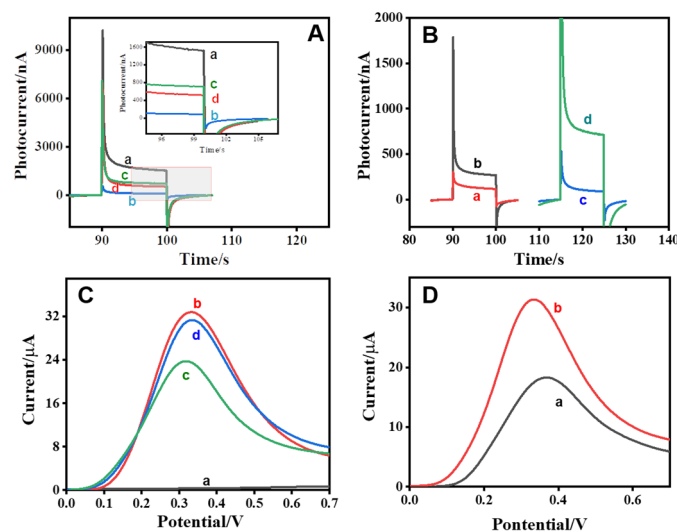
Figure 4. (**A**) Photocurrent response of the (a) Bi_2S_3/MXene, (b) MIP-CGA/Bi_2S_3/MXene, (c) MIP/Bi_2S_3/MXene and (d) MIP/ Bi_2S_3/MXene in presence of 2.825×10^{-7} M CGA; (**B**) Photocurrent response of (a,b) NIP/Bi_2S_3/MXene and (c,d) MIP/Bi_2S_3/MXene before (b,d) and after (a,c) CGA elution, respectively; (**C**) DPV response of (a) Bi_2S_3/MXene, (b) MIP-CGA/Bi_2S_3/MXene, (c) MIP/B Bi_2S_3/MXene and (d) MIP/Bi_2S_3/MXene in presence of 2.825×10^{-7} M CGA; (**D**) DPV response of (a) FTO and (b) Bi_2S_3/MXene/FTO in presence of 2.825×10^{-7} M CGA.

3.4. Optimization of Experimental Conditions

To improve the performance of the proposed sensor for CGA detection, some experimental parameters were optimized, including $Ti_3C_2T_X$ MXene ratio, the concentration of Bi_2S_3/MXene, the ratio of elution solution, elution time and MIP volume. The MXene ratio increased from 3% to 10%, the photocurrent response increased significantly in Figure S3A. However, it decreased slightly when $Ti_3C_2T_X$ MXene ratio exceeded 10%. Thus, 10% $Ti_3C_2T_X$ MXene ratio was implemented as substrate material. Then, the concentrations of Bi_2S_3/MXene were thoroughly investigated. As shown in Figure S3B, too low or too high concentration of Bi_2S_3/MXene would affect the electronic conduction, indicating the excess Bi_2S_3/MXene suppressed photo-generated electron-hole conversion. The optimal concentration of Bi_2S_3/MXene was 5 mg mL^{-1} for the experiment.

The elution efficiency of MIP with different ratios of eluents was investigated in Figure S3C. Under the same conditions, the elution efficiency with 10% ethanol was the most obvious. As the concentration of the eluent increased, the number of the eluent cavity also increased. However, when the concentration of the eluent was too high, the MIP layer formed by the polymerization could be damaged by the eluent. Therefore, 10% ethanol was selected as the eluent. Besides, elution time also affected the number of cavities formed by the imprinted layer. As shown in Figure S3D, the elution time increased from 10 min to 30 min, and the photocurrent response increased. After elution for 30 min, the PEC response decreased significantly. The elution time might be too short, leading to incomplete elution. Since the elution time was too long, the MIP layer would fall off in the eluent. Therefore, 30 min was selected as the elution time.

Figure S3E showed the influence of MIP volume on the sensing performance. The photocurrent changes of 20 μL MIP were the most obvious. This could be attributed to the small volume MIP with fewer CGA molecules, resulting in little changes in the photocurrent before and after elution. When the volume reached 20 μL, more cavities were eluted, and the intensity of photocurrent increased. If larger than 20 μL, the size of the MIP might be too large to impede electron conduction. In summary, the dosage of 20 μL MIP was taken as the optimal experimental condition.

3.5. Performance of the PEC/EC Dual-Mode Sensing of CGA

To evaluate the performance of the fabricated dual-signal sensing platform, PEC measurement was first carried out. Figure 5A showed the remarkable photocurrent reduction with the concentration of CGA, because the specific molecular recognition sites of MIP/Bi_2S_3/$Ti_3C_2T_X$ MXene/FTO could specifically adsorb CGA, which lead to the hindering of the electron transfer of Bi_2S_3/$Ti_3C_2T_X$ MXene. With the increasing concentration of CGA from 2.825×10^{-8} M to 2.825×10^{-5} M, the PEC signal showed a downward trend, which was attributed to the recombination of CGA with the cavity impeding electron transport. The regression equation of the calibration curve was $I = 820.821 - 197.479 \lg C_{CGA}$ ($R^2 = 0.995$), and detection limit (LOD) was 2.4 nM (Figure 5B). In addition, the DPV measurement was also applied to the CGA detection. The specific molecular recognition capability of MIP/Bi_2S_3/$Ti_3C_2T_X$ MXene/FTO for CGA made a remarkable difference in the DPV signal, indicating that Bi_2S_3/$Ti_3C_2T_X$ MXene had preferable electrochemical catalytic activity for redox of CGA. As shown in Figure 5C, the DPV responses showed an upward trend with the increase of CGA concentrations, and this trend mainly depended on the electrocatalytic activity of CGA in Bi_2S_3/MXene/MIP. Figure 5D showed a good linear relationship related to logarithmic values of CGA concentrations from 1.412×10^{-7} M to 2.259×10^{-5} M. The linear equation was $I = 4.536 \lg C_{CGA} + 17.318$ ($R^2 = 0.997$). The LOD of CGA concentration was calculated to be 43.1 nM. The fabricated dual-mode sensing platform had a wider linear range and lower detection limits than previously reported CGA concentration detection methods (Table 1).
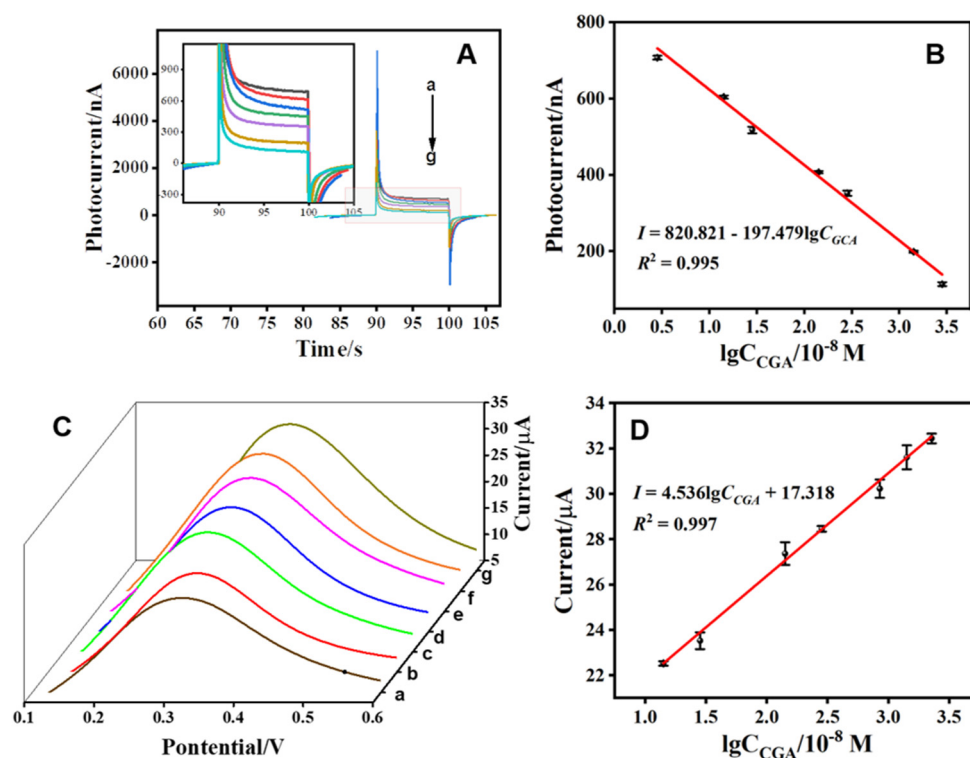

Figure 5. (**A**) Photocurrent response of different concentrations of CGA: (a) 2.825×10^{-8} mol L^{-1}, (b) 1.412×10^{-7} mol L^{-1}, (c) 2.825×10^{-7} mol L^{-1}, (d) 1.412×10^{-6} mol L^{-1}, (e) 2.825×10^{-6} mol L^{-1}, (f) 1.412×10^{-5} mol L^{-1}, (g) 2.825×10^{-5} mol L^{-1}; (**B**) Its corresponding calibration curve of biosensor platform; (**C**) DPV response of different concentration of CGA: (a) 1.412×10^{-7} mol L^{-1}, (b) 2.825×10^{-7} mol L^{-1}, (c) 1.412×10^{-6} mol L^{-1}, (d) 2.825×10^{-6} mol L^{-1}, (e) 8.475×10^{-6} mol L^{-1}, (f) 1.412×10^{-5} mol L^{-1} and (g) 2.259×10^{-5} mol L^{-1}; (**D**) The corresponding calibration curve.

Table 1. Comparison of the different approaches for determining CGA.

Method	Linear Range (μmol L^{-1})	LOD (μmol L^{-1})	Ref.
MEKC	71–2500	2.77	[50]
FTCP	5–100	0.57	[56]
EC	0.01–13.0	0.007	[57]
Voltammetry	5.64–147	1.26	[58]
CDs	1.53–80	0.46	[59]
PEC-EC	0.0282–2824(PEC) 0.1412–22.59(EC)	0.0024 0.0431	This work

3.6. Selectivity and Stability of the PEC Sensor

To verify the selectivity of the constructed PEC/EC dual-mode sensing platform, some similar substances were used as interference substances of CGA. The interference mixture solution was performed in a 2.825×10^{-7} mol L^{-1} CGA solution by adding L-Lysine, L-Histidine, L-Cysteine, Urea and NaCl. In addition, the selectivity of the constructed sensor was investigated by $R(\%)$ calculation ($R\% = |(I_0 - I_1)/(I_0 - I_2)| \times 100\%$). As shown in Figure 6A, where I_0 was the signal in 0.1 M PBS solution without CGA, I_1 represented the response signal of Bi$_2$S$_3$/MXene/MIP electrode in interfering specifics solution and I_2 is the signal in 2.825×10^{-7} M CGA. As illustrated in Figure 6A, due to the imprinting effect of the molecularly imprinted layer, the EC and PEC responses of the dual-mode sensor for CGA were larger than those of the interferents, indicating that the selectivity of the designed sensor had a high performance. Furthermore, to verify the stability of the proposed PEC sensor, the photocurrent was tested by repeated "on-off" irradiation 10 times within 200 s [60,61], as shown in Figure 6B. Surprisingly, the sensor exhibited good stability after 10 cycles of light irradiation and the relative standard deviations (RSD) was 6.38%.
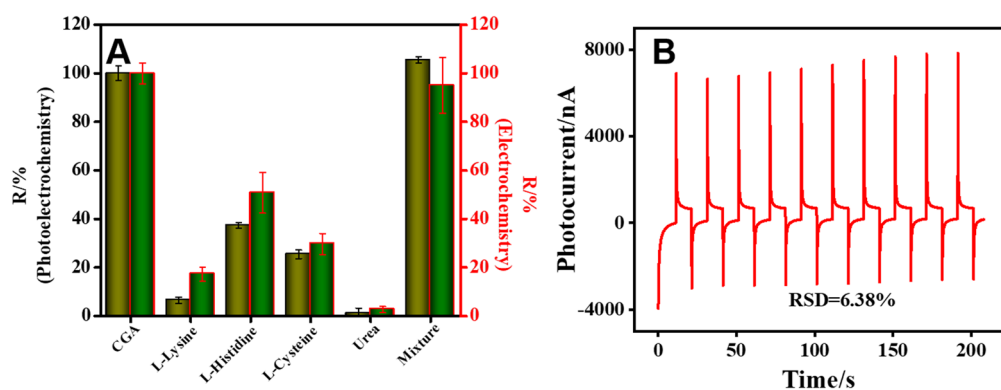

Figure 6. (**A**) Selectivity of the PEC/EC dual-mode sensor for CGA (2.825×10^{-7} mol L^{-1}) compared with interferences including L-Lysine, L-Histidine, L-Cysteine, Urea and their mixtures; (**B**) Stability of the constructed PEC sensor towards 2.825×10^{-7} mol L^{-1} CGA.

3.7. Real Sample Analysis

To evaluate the practical application of the dual-mode sensor platform, we simulated the real samples (tea, juice and coffee) for CGA detection. The simulative tea samples were prepared by adding 0.5 g tea and 50 mL ultrapure water into a beaker, then heated and stirred at 60 °C for 30 min. Then, the tea, juice and coffee samples were pretreated by filtration membrane (0.22 μm). Different concentrations of CGA (0.28 μmol L^{-1}, 1.42 μmol L^{-1} and 2.82 μmol L^{-1}) were injected into the above filtered tea, juice and coffee solution, respectively. Table 2 showed the recovery rate of simulated samples ranging from 91.33% to 108.70%, and the RSD did not exceed 7%. The results demonstrated that the dual-signal sensor had a good potential in simulating the detection in tea, juice and coffee samples, and was expected to realize the detection of CGA in other foods.

Table 2. Detection of real samples by the dual-mode sensor platform.

Matrice	Sample No.	Spiked Con. (μmol L^{-1})	PEC Detected Con. (μmol L^{-1})	PEC Recovery%	PEC RSD%	EC Detected Con. (μmol L^{-1})	EC Recovery%	EC RSD%
Tea	1	0.28	0.2692	96.14	0.89	0.3012	107.57	6.54
	2	1.41	1.4943	105.98	4.48	1.5327	108.70	2.13
	3	2.82	2.6611	94.37	3.26	2.7141	96.25	3.38
Juice	4	0.28	0.2910	103.92	1.56	0.3039	108.54	0.15
	5	1.41	1.3752	97.53	2.05	1.3423	95.20	3.20
	6	2.82	2.7120	96.17	2.30	2.5755	91.33	5.41
Coffee	7	0.28	0.2774	99.06	6.84	0.2696	96.29	0.89
	8	1.41	1.4665	104.01	4.85	1.3550	96.10	0.64
	9	2.82	2.8623	101.50	2.36	2.9565	104.84	4.62

4. Conclusions

In summary, we developed a MIP functionalized $Bi_2S_3/Ti_3C_2T_X$ MXene nanocomposite to construct a PEC/EC sensing platform, and realized the dual-signal detection of CGA. The higher photoelectric conversion efficiency of $Bi_2S_3/Ti_3C_2T_X$ MXene not only provided a PEC signal with a high background, but also had electrocatalytic capability. With CGA as a concept target and $Bi_2S_3/Ti_3C_2T_X$ MXene as the photoactive material, a fast and highly sensitive PEC sensor was constructed by combining molecular imprinting technology. The integration of EC and PEC sensors was conducive to quickly decide whether target analytes existed. In addition, compared to single signal detection, PEC and EC signals could be used as a mutual reference to improve reliability and accuracy, and provided more comprehensive information. Importantly, this sensing strategy provided a new idea that might be generalized for the construction of other dual-signal detection platforms with electrochemical signal substances.

References

1. Shu, J.; Tang, D. Recent advances in photoelectrochemical sensing: From engineered photoactive materials to sensing devices and detection modes. *Anal. Chem.* **2020**, *92*, 363–377. [CrossRef]
2. Qiu, Z.; Tang, D. Nanostructures-based photoelectrochemical sensing platforms for biomedical applications. *J. Mater. Chem. B* **2020**, *8*, 2541–2561. [CrossRef]

3. Zhou, Q.; Tang, D. Recent advances in photoelectrochemical biosensors for analysis of mycotoxins in food. *TRAC Trends Anal. Chem.* **2020**, *124*, 115814. [CrossRef]

4. Shu, J.; Tang, D. Current advances in quantum dots-based photoelectrochemical immunoassays. *Chem. Asian J.* **2017**, *12*, 2780–2789. [CrossRef]

5. Zhao, W.W.; Xu, J.J.; Chen, H.Y. Photoelectrochemical enzymatic biosensors. *Biosens. Bioelectron.* **2017**, *92*, 294–304. [CrossRef]

6. Liu, Y.; Wei, Z.; Zhou, J.; Ma, Z. Simultaneous multi-signal quantification for highly precise serodiagnosis utilizing a rationally constructed platform. *Nat. Commun.* **2019**, *10*, 1–10. [CrossRef]

7. Zhu, M.J.; Pan, J.B.; Wu, Z.Q.; Gao, X.Y.; Zhao, W.; Xia, X.H.; Xu, J.J.; Chen, H.Y. Electrogenerated chemiluminescence imaging of electrocatalysis at a single Au-Pt janus nanoparticle. *Angew. Chem.* **2018**, *57*, 4074–4078. [CrossRef]

8. Xue, J.; Zhao, Q.; Yang, L.; Ma, H.; Wu, D.; Liu, L.; Ren, X.; Ju, H.; Wei, Q. Dual-mode sensing platform guided by intramolecular electrochemiluminescence of a ruthenium complex and cationic N, N-bis(2-(trimethylammonium iodide)propylene) perylene-3,4,9,10-tetracarboxydiimide for estradiol assay. *Anal. Chem.* **2021**, *93*, 6088–6093. [CrossRef]

9. Hu, Y.; Zhu, L.; Mei, X.; Liu, J.; Yao, Z.; Li, Y. Dual-mode sensing platform for electrochemiluminescence and colorimetry detection based on a closed bipolar electrode. *Anal. Chem.* **2021**, *93*, 12367–12373. [CrossRef]

10. Han, Q.; Zhao, X.; Na, N.; Ouyang, J. Integrating near-infrared visual fluorescence with a photoelectrochemical sensing system for dual readout detection of biomolecules. *Anal. Chem.* **2021**, *93*, 3486–3492. [CrossRef]

11. Wei, J.; Chang, W.; Qileng, A.; Liu, W.; Zhang, Y.; Rong, S.; Lei, H.; Liu, Y. Dual-modal split-type immunosensor for sensitive detection of microcystin-LR: Enzyme-induced photoelectrochemistry and colorimetry. *Anal. Chem.* **2018**, *90*, 9606–9613. [CrossRef]

12. Yu, Z.; Gong, H.; Li, Y.; Xu, J.; Zhang, J.; Zeng, Y.; Liu, X.; Tang, D. Chemiluminescence-derived self-powered photoelectrochemical immunoassay for detecting low-abundance disease-related protein. *Anal. Chem.* **2021**, *93*, 13389–13397. [CrossRef]

13. Qiu, Z.; Shu, J.; Liu, J.; Tang, D. Dual-channel photoelectrochemical ratiometric aptasensor with up-converting nanocrystals using spatial-resolved technique on homemade 3D printed device. *Anal. Chem.* **2019**, *91*, 1260–1268. [CrossRef]

14. Zeng, R.; Gong, H.; Li, Y.; Li, Y.; Lin, W.; Tang, D.; Knopp, D. CRISPR-Cas12a-derived photoelectrochemical biosensor for point-of-care diagnosis of nucleic acid. *Anal. Chem.* **2022**, *94*, 7442–7448. [CrossRef]

15. Hu, C.-L.; Pan, H.-J.; Ma, R.-N.; Cheng, S.; Jia, L.-P.; Zhang, W.; Shang, L.; Xue, Q.-W.; Wei, Q.; Wang, H.-S. Gold nanoparticle-attached perovskite $Cs_3Bi_2Br_9$ QDs/BiOBr heterostructures for photoelectrochemical biosensing. *ACS Appl. Nano Mater.* **2022**, *5*, 2812–2819. [CrossRef]

16. Tan, X.; Yu, H.; Liang, B.; Han, M.; Ge, S.; Zhang, L.; Li, L.; Li, L.; Yu, J. A target-driven self-feedback paper-based photoelectrochemical sensing platform for ultrasensitive detection of ochratoxin A with an In_2S_3/WO_3 heterojunction structure. *Anal. Chem.* **2022**, *94*, 1705–1712. [CrossRef]

17. Qiu, Z.; Shu, J.; Tang, D. $NaYF_4$:Yb, Er upconversion nanotransducer with in situ fabrication of Ag_2S for near-infrared light responsive photoelectrochemical biosensor. *Anal. Chem.* **2018**, *90*, 12214–12220. [CrossRef]

18. Petrucci, R.; Bortolami, M.; Di Matteo, P.; Curulli, A. Gold nanomaterials-based electrochemical sensors and biosensors for phenolic antioxidants detection: Recent advances. *Nanomaterials* **2022**, *12*, 959. [CrossRef]

19. Song, Y.; Luo, Y.; Zhu, C.; Li, H.; Du, D.; Lin, Y. Recent advances in electrochemical biosensors based on graphene two-dimensional nanomaterials. *Biosens. Bioelectron.* **2016**, *76*, 195–212. [CrossRef]

20. Hu, R.; Zhang, X.; Chi, K.-N.; Yang, T.; Yang, Y.-H. Bifunctional MOFs-based ratiometric electrochemical sensor for multiplex heavy metal ions. *ACS Appl. Mater. Interfaces* **2020**, *12*, 30770–30778. [CrossRef]

21. Zeng, R.; Wang, W.; Chen, M.; Wan, Q.; Wang, C.; Knopp, D.; Tang, D. CRISPR-Cas12a-driven MXene-PEDOT:PSS piezoresistive wireless biosensor. *Nano Energy* **2021**, *82*, 105711. [CrossRef]

22. Cai, G.; Yu, Z.; Tong, P.; Tang, D. Ti_3C_2 MXene quantum dots-encapsulated liposome for photothermal immunoassay using a portable near-infrared imaging camera on smartphone. *Nanoscale* **2019**, *11*, 15659–15667. [CrossRef]

23. Liu, L.; Yao, Y.; Ma, K.; Shangguan, C.; Jiao, S.; Zhu, S.; Xu, X. Ultrasensitive photoelectrochemical detection of cancer-related miRNA-141 by carrier recombination inhibition in hierarchical $Ti_3C_2@ReS_2$. *Sens. Actuators B Chem.* **2021**, *331*, 129470. [CrossRef]

24. Helal, A.; Harraz, F.A.; Ismail, A.A.; Sami, T.M.; Ibrahim, A. Hydrothermal synthesis of novel heterostructured Fe2O3/Bi2S3 nanorods with enhanced photocatalytic activity under visible light. *Appl. Catal. B* **2017**, *213*, 18–27. [CrossRef]

25. Qiu, Z.; Shu, J.; Tang, D. Near-infrared-to-ultraviolet light-mediated photoelectrochemical aptasensing platform for cancer biomarker based on core-shell $NaYF_4$: Yb,Tm@TiO$_2$ upconversion microrods. *Anal. Chem.* **2018**, *90*, 1021–1028. [CrossRef] [PubMed]

26. BelBruno, J.J. Molecularly imprinted polymers. *Chem. Rev.* **2019**, *119*, 94–119. [CrossRef]

27. Chen, L.X.; Wang, X.Y.; Lu, W.H.; Wu, X.Q.; Li, J.H. Molecular imprinting: Perspectives and applications. *Chem. Soc. Rev.* **2016**, *45*, 2137–2211. [CrossRef]

28. Bhogal, S.; Kaur, K.; Malik, A.K.; Sonne, C.; Lee, S.S.; Kim, K.H. Core-shell structured molecularly imprinted materials for sensing applications. *TrAC Trends Anal. Chem.* **2020**, *133*, 116043. [CrossRef]

29. Yang, X.; Gao, Y.; Ji, Z.; Zhu, L.B.; Yang, C.; Zhao, Y.; Shu, Y.; Jin, D.; Xu, Q.; Zhao., W.W. Dual functional molecular imprinted polymers-modified organometal lead halide perovskite: Synthesis and application for photoelectrochemical sensing of salicylic acid. *Anal. Chem.* **2019**, *91*, 9356–9360. [CrossRef]

30. Tong, P.; Zhang, L.; He, Y.; Chi, Y.W.; Chen, G.N. A simple capillary electrophoresis with electrochemical detection method for determination of the hydrolysis rate constant of chlorogenic acid. *Talanta* **2009**, *77*, 1790–1794. [CrossRef]

31. Yang, S.P.; Han, Y.Z.; Wang, K.R.; Wang, Y.; Li, L.P.; Li, N.; Xu, X.D. Simultaneous determination of four phenolic acids in traditional Chinese medicine by capillary electrophoresis-chemiluminescence. *RSC Adv.* **2021**, *11*, 33996–34003. [CrossRef] [PubMed]

32. Lin, H.; Wang, X.; Yu, L.; Chen, Y.; Shi, J. Two-dimensional ultrathin MXene ceramic nanosheets for photothermal conversion. *Nano Lett.* **2017**, *17*, 384–391. [CrossRef] [PubMed]

33. Lu, L.; Han, X.; Lin, J.; Zhang, Y.; Qiu, M.; Chen, Y.; Li, M.; Tang, D. Ultrasensitive fluorometric biosensor based on Ti$_3$C$_2$ MXenes with Hg^{2+}-triggered exonuclease III-assisted recycling amplification. *Analyst* **2021**, *146*, 2664–2669. [CrossRef]

34. Li, J.F.; Li, Z.Y.; Liu, X.M.; Li, C.Y.; Zheng, Y.F.; Yeung, K.W.K.; Cui, Z.D.; Liang, Y.Q.; Zhu, S.L.; Hu, W.B.; et al. Interfacial engineering of Bi$_2$S$_3$/Ti$_3$C$_2$T$_X$ MXene based on work function for rapid photo-excited bacteria-killing. *Nat. Commun.* **2021**, *12*, 1–10. [CrossRef]

35. Zou, Z.; Wang, Q.; Zhu, K.; Ye, K.; Wang, G.; Cao, D.; Yan, J. Ultrathin-walled Bi$_2$S$_3$ nanoroll/MXene composite toward high capacity and fast lithium storage. *Small* **2022**, *18*, 2106673. [CrossRef]

36. Liu, Q.Q.; Zhao, Y.; Pan, J.F.; Van der Bruggen, B.; Shen, J.N. A novel chitosan base molecularly imprinted membrane for selective separation of chlorogenic acid. *Sep. Purif. Technol.* **2016**, *164*, 70–80. [CrossRef]

37. Wang, Y.; Wang, E.; Wu, Z.; Li, H.; Zhu, Z.; Zhu, X.; Dong, Y. Synthesis of chitosan molecularly imprinted polymers for solidphase extraction of methandrostenolone. *Carbohyd. Polym.* **2014**, *101*, 517–523. [CrossRef]

38. Agresti, A.; Pazniak, A.; Pescetelli, S.; Di Vito, A.; Rossi, D.; Pecchia, A.; Auf der Maur, M.; Liedl, A.; Larciprete, R.; Kuznetsov, D.V.; et al. Titanium-carbide MXenes for work function and interface engineering in perovskite solar cells. *Nat. Mater.* **2019**, *18*, 1228–1234. [CrossRef]

39. Liao, Y.; Qian, J.; Xie, G.; Han, Q.; Dang, W.Q.; Wang, Y.S.; Lv, L.L.; Zhao, S.; Luo, L.; Zhang, W.; et al. 2D-layered Ti$_3$C$_2$ MXenes for promoted synthesis of NH$_3$ on P25 photocatalysts. *Appl. Catal. B* **2020**, *273*, 119054. [CrossRef]

40. Ni, J.F.; Zhao, Y.; Liu, T.T.; Zheng, H.H.; Gao, L.J.; Yan, C.L.; Li, L. Strongly Coupled Bi$_2$S$_3$@CNT Hybrids for Robust Lithium Storage. *Adv. Energy Mater.* **2014**, *4*, 1400798. [CrossRef]

41. Liu, Y.; Zhang, M.; Li, L.; Zhang, X. In situ ion exchange synthesis of the Bi$_4$Ti$_3$O$_{12}$/Bi$_2$S$_3$ heterostructure with enhanced photocatalytic activity. *Catal. Commun.* **2015**, *60*, 23–26. [CrossRef]

42. Wu, G.; Li, T.; Wang, Z.; Li, M.; Wang, B.; Dong, A. Molecular ligand-mediated assembly of multicomponent nanosheet superlattices for compact capacitive energy storage. *Angew. Chem. Int. Ed.* **2020**, *59*, 20628. [CrossRef] [PubMed]

43. Tang, X.W.; Murali, G.; Lee, H.; Park, S.; Lee, S.; Oh, S.M.; Lee, J.; Ko, T.Y.; Koo, C.M.; Jeong, Y.J.; et al. Engineering Aggregation-Resistant MXene Nanosheets As Highly Conductive and Stable Inks for All-Printed Electronics. *Adv. Funct. Mater.* **2021**, *31*, 2010897. [CrossRef]

44. Fu, Y.; Ding, F.; Chen, J.; Liu, M.; Zhang, X.; Dua, C.; Si, S. Label-free and near-zero-background-noise photoelectrochemical assay of methyltransferase activity based on a Bi$_2$S$_3$/Ti$_3$C$_2$ Schottky junction. *Chem. Commun.* **2020**, *56*, 5799–5802. [CrossRef] [PubMed]

45. Abdi, F.F.; Han, L.; Smets, A.H.M.; Zeman, M.; Dam, B.; van de Krol, R. Efficient solar water splitting by enhanced charge separation in a bismuth vanadate-silicon tandem photoelectrode. *Nat. Commun.* **2013**, *4*, 2195. [CrossRef]

46. Ahmmed, S.; Aktar, A.; Hossain, J.; Ismail, A.B.M. Enhancing the open circuit voltage of the SnS based heterojunction solar cell using NiO HTL. *Sol. Energy* **2020**, *207*, 693–702. [CrossRef]

47. Xiao, D.; Li, X.; Wang, D.; Li, Q.; Shen, K.; Wang, D. CdTe thin film solar cell with NiO as a back contact buffer layer. *Sol. Energy Mater. Sol. Cells* **2017**, *169*, 61–67. [CrossRef]

48. Ghane, N.; Sadrnezhaad, S.K.; Hosseini, H.S.M. Combustion synthesis of g-C$_3$N$_4$/Fe$_2$O$_3$ nanocomposite for superior photoelectrochemical catalytic performance. *Appl. Surf. Sci.* **2020**, *534*, 147563. [CrossRef]

49. Liu, J.; Lu, J.F.; Kan, J.; Jin, C.H. Synthesis of chitosan-gallic acid conjugate: Structure characterization and in vitro anti-diabetic potential. *Int. J. Biol. Macromol.* **2013**, *62*, 321–329. [CrossRef]

50. Risso, E.M.; Péres, R.G.; Amaya-Farfan, J. Determination of phenolic acids in coffee by micellar electrokinetic chromatography. *Food Chem.* **2007**, *105*, 1578–1582. [CrossRef]

51. Cui, Z.; Xiang, Y.; Si, J.; Yang, M.; Zhang, Q.; Zhang, T. Ionic interactions between sulfuric acid and chitosan membranes. *Carbohyd. Polym.* **2008**, *73*, 111–116. [CrossRef]

52. Kamari, A.; Ngah, W.S.W.; Chong, M.Y.; Cheah, M.L. Sorption of acid dyes onto GLA and H$_2$SO$_4$ cross-linked chitosan beads. *Desalination* **2009**, *249*, 1180–1189. [CrossRef]

53. Wang, C.; Ye, X.; Wang, Z.; Wu, T.; Wang, Y.; Li, C. Molecularly imprinted photoelectrochemical sensor for human epididymis protein 4 based on polymerized ionic liquid hydrogel and gold nanoparticle/ZnCdHgSe QDs composite film. *Anal. Chem.* **2017**, *89*, 12391–12398. [CrossRef]

54. Zhao, X.; Bai, J.; Bo, X.; Guo, L. A novel electrochemical sensor based on 2D CuTCPP nanosheets and platelet ordered mesoporous carbon composites for hydroxylamine and chlorogenic acid. *Anal. Chim. Acta* **2019**, *1075*, 71–80. [CrossRef] [PubMed]

55. Chen, Y.; Huang, W.; Chen, K.; Zhang, T.; Wang, Y.; Wang, J. A novel electrochemical sensor based on core-shell-structured metal-organic frameworks: The outstanding analytical performance towards chlorogenic acid. *Talanta* **2019**, *196*, 85–91. [CrossRef]

56. Tomac, I.; Šeruga, M.; Beinrohr, E. Characterization of chlorogenic acids in coffee by flow-through chronopotentiometry. *Food Anal. Method* **2017**, *10*, 3924–3933. [CrossRef]

57. Wang, Y.; Chen, H.H.; Hu, X.Y.; Yu, H. Highly stable and ultrasensitive chlorogenic acid sensor based on metal-organic frameworks/titanium dioxide nanocomposites. *Analyst* **2016**, *141*, 4647–4653. [CrossRef]
58. Yardım, Y.; Keskin, E.; Şentürk, Z. Voltammetric determination of mixtures of caffeine and chlorogenic acid in beverage samples using a boron-doped diamond electrode. *Talanta* **2013**, *116*, 1010–1017. [CrossRef]
59. Han, Z.; He, L.; Pan, S.; Liu, H.; Hu, X.L. Hydrothermal synthesis of carbon dots and their application for detection of chlorogenic acid. *Luminescence* **2020**, *35*, 989–997. [CrossRef]
60. Gao, Y.; Zeng, Y.; Liu, X.; Tang, D. Liposome-mediated in situ formation of type-I heterojunction for amplified photoelectrochemical immunoassay. *Anal. Chem.* **2022**, *94*, 4859–4865. [CrossRef]
61. Yu, Z.; Gong, H.; Xu, J.; Li, Y.; Zeng, Y.; Liu, X.; Tang, D. Exploiting photoelectric activities and piezoelectric properties of $NaNbO_3$ semiconductors for point-of-care immunoassay. *Anal. Chem.* **2022**, *94*, 3418–3426. [CrossRef] [PubMed]